NiVCe-Layered Double Hydroxide as Multifunctional Nanomaterials for Energy and Sensor Applications

Josué M. Gonçalves[1]*, Irlan S. Lima[1], Nathália F. B. Azeredo[1], Diego P. Rocha[1], Abner de Siervo[2] and Lúcio Angnes[1]*

[1]Department of Fundamental Chemistry, Institute of Chemistry, Universidade de São Paulo, São Paulo, Brazil, [2]Applied Physics Department, Institute of Physics "Gleb Wataghin", State University of Campinas, Campinas, Brazil

Multifunctional nanomaterials have been attracting increasing attention as solutions to the existing challenges in energy systems and sensing technologies. In this regard, multifunctional NiVCe-layered double hydroxide (NiVCe-LDH) nanoparticles were synthesized by the modified sol-gel method. The analysis of this material demonstrated excellent potential for its utilization as electrode materials for hybrid supercapacitor, oxygen evolution reaction (OER), and sensor applications. The NiVCe-LDH nanoparticles delivered a specific charge of $740 \, C \, g^{-1}$ at $10 \, A \, g^{-1}$ and decent rate performance (charge retention of 68.7% at $100 \, A \, g^{-1}$), showing excellent prospects as electrode material for hybrid energy storage devices. In addition, NiVCe-LDH nanoparticles have also been successfully applied as a proof-of-concept for OER, as confirmed by their low Tafel slope of $47 \, mV \, dec^{-1}$. Finally, trimetallic NiVCe-LDH-based screen-printed electrodes were developed for the sensing of hydrogen peroxide directly in a real complex mouthwash sample, achieving a satisfactory recovery value of around 98% using a fast and simple batch injection analysis procedure. These results allow us to predict the great potential of this trimetallic hydroxide for building electrochemical sensors with good perspectives as electroactive material for OER processes and energy storage technologies.

Keywords: layered double hydroxides (LDH), multifunctional, electrocatalyst, oxygen evolution reaction (OER), hybrid supercapacitor, electrochemical sensor

INTRODUCTION

Transition metal-containing layered double hydroxides (LDHs) have emerged as multifunctional inorganic nanomaterials with large specific surface area, remarkable mechanical properties, and tunable electric and thermal conductivity (Tomboc et al., 2021). In fact, these LDH-based nanomaterials with their extraordinary inherent properties have become potential candidates for several scientific and technological challenges for a more sustainable society. They are excellent candidates for electrochemical energy conversion and storage systems (Shao et al., 2015; Gonçalves et al., 2020a; Gonçalves et al., 2020b), as well as catalytic materials in electrochemical sensors (Rossini et al., 2020).

In fact, the high dispersion of active species in a layered structure, the exfoliation process, and chemical modification open new opportunities for the development of LDHs as multifunctional electrodes materials (Shao et al., 2015). For instance, recently, our group reviewed the late signs of
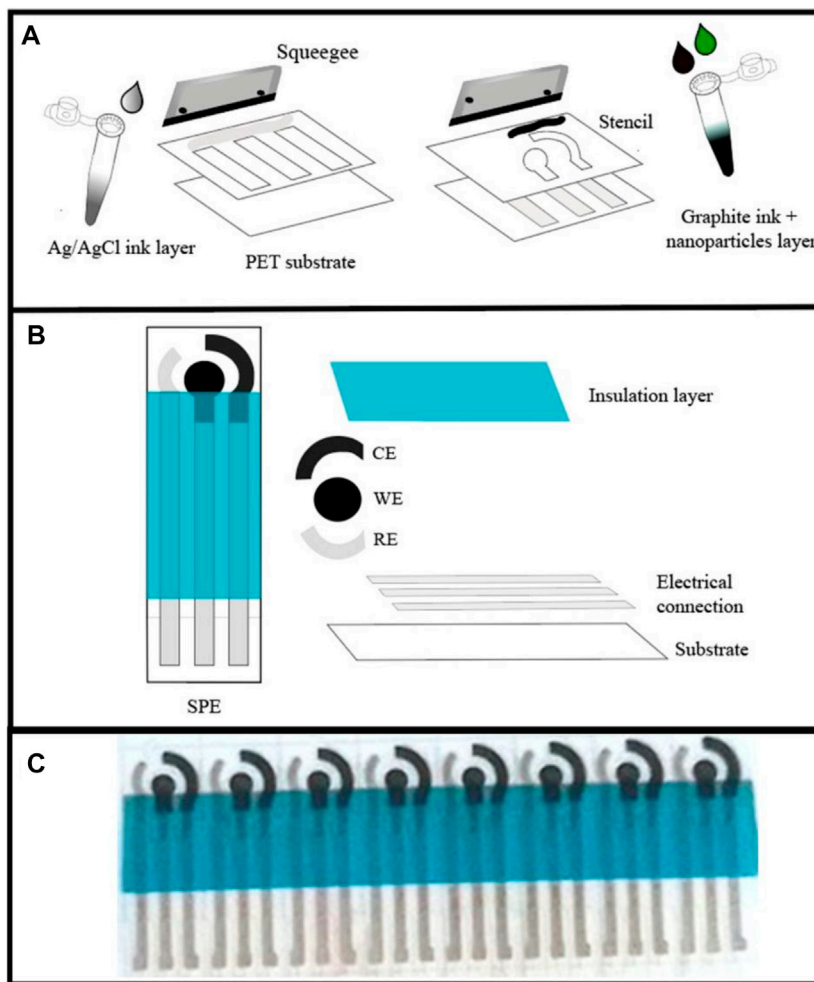
SCHEME 1 | (A) Fabrication of screen-printed electrode and its coating with graphite ink loaded with 25% (in weight) of $Ni_{0.9}Ce_{0.05}V_{0.05}$-LDH NPs. **(B)** A design drawing and **(C)** photography of electrochemical analytical devices with three-electrodes developed using screen printing.
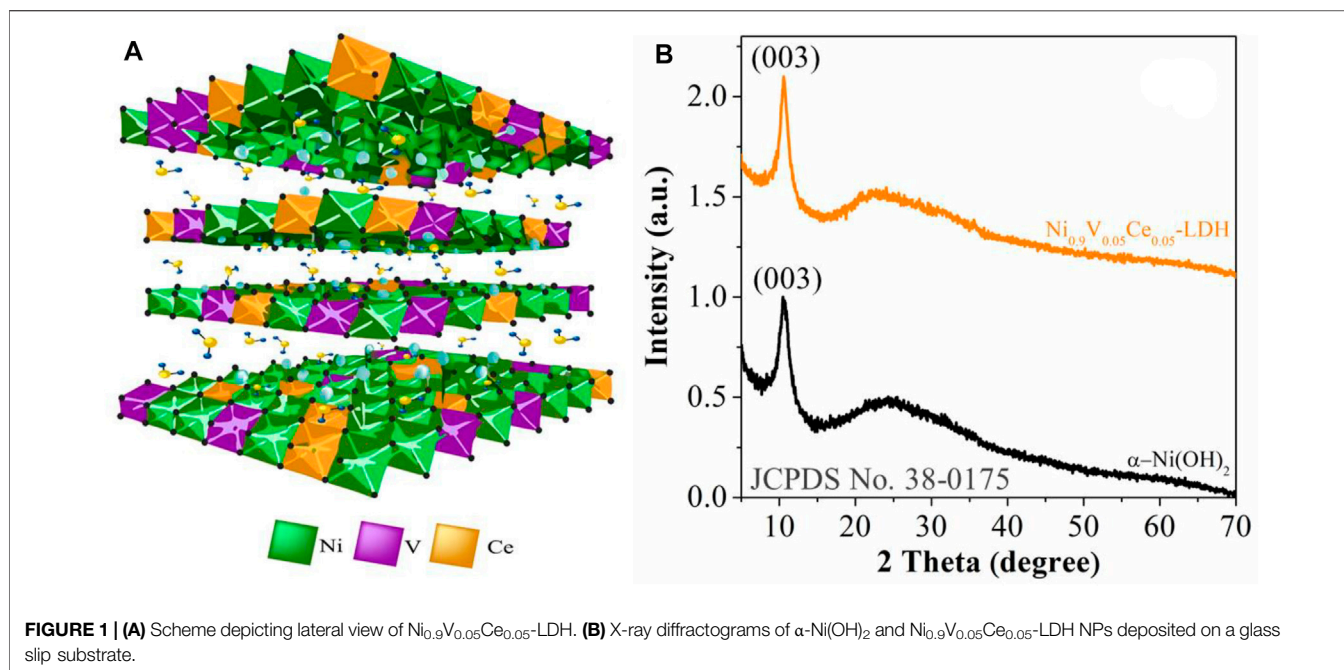
progress and trends for the design of electrocatalysts with the potential to surpass the sluggish kinetics and the high activation energy barrier for multistep electron transfer processes of the oxygen evolution reaction (OER) (Gonçalves et al., 2020a), as well as in the preparation of electrode materials for hybrid supercapacitors (HSCs) (Gonçalves et al., 2020b). For both cases, the preparation of trimetallic LDHs has been an excellent strategy for improving the electrochemical properties of these promising materials.

In this sense, Xu et al. (2018) reported a facile and low-cost *in situ* self-assembly strategy for preparing a hierarchical nanocomposite based on Ce-doped NiFe-LDH nanosheets and carbon nanotube (CNT), denoted as NiFeCe-LDH/CNT. Further experimental results indicate that doped Ce into NiFe-LDH/CNT nanoarrays electrocatalyst showed highly efficient OER activity with a low overpotential (227 mV required for 10 mA cm^{-2}) and Tafel slope (33 mV dec^{-1}) in alkaline medium, showing to compete favorably against the reported NiFe-based LDHs. According to the authors, the doping

process with Ce^{3+} may create lattice defects in the NiFe-LDH and promote electron interactions between the LDH-derived and the CNTs, improving the electrocatalytic performance.

The formation of LDHs by the incorporation of Ce^{3+} has also been a strategy in the development of sensors (Gonçalves et al., 2017; Azeredo et al., 2021) and electrocatalysts for oxidation reactions (Assis et al., 2020). For instance, Gonçalves et al. (2017) developed nickel-based hydroxide nanoparticles (NPs) with enhanced electrocatalytic activity and stability by incorporation of 20 atom% of Ce$^{3+/4+}$ ions (Ni$_{0.8}$Ce$_{0.2}$-LDH). The Ni$_{0.8}$Ce$_{0.2}$-LDH was constituted by smaller NPs as compared with pristine Ni(OH)$_2$. As a result, a sensitive sensor for prednisone was manufactured exploring the electrocatalytic oxidation reaction, achieving a sensitivity value as high as 3.9 × 10^{-2} A M^{-1} cm^{-2} and a limit of detection (LOD) as low as 8.4 × 10^{-9} mol L^{-1} under flow injection analysis.

In addition to Ce^{3+} ions, the incorporation of vanadium ions in the preparation of bi- (Zhou et al., 2018; Liu et al., 2019; He

FIGURE 1 | (A) Scheme depicting lateral view of $Ni_{0.9}V_{0.05}Ce_{0.05}$-LDH. **(B)** X-ray diffractograms of α-Ni(OH)$_2$ and $Ni_{0.9}V_{0.05}Ce_{0.05}$-LDH NPs deposited on a glass slip substrate.

et al., 2020) and trimetallic (Dinh et al., 2018; Li et al., 2018; Arif et al., 2020) LDHs has also been quite reported, not only for the development of electrocatalysts for OER (Gonçalves et al., 2020c; Gonçalves et al., 2021) but also for HSCs (Gonçalves et al., 2021). For example, Wang et al. (2019a) reported a series of NiVFe-LDH through a one-step coprecipitation method. Among them, the $Ni_3V_1Fe_1$-LDH showed a better OER performance displaying a low overpotential of 269 mV at 10 mA cm^{-2} in 1.0-M potassium hydroxide (KOH) solution and a small Tafel slope (68 mV dec^{-1}), indicating that V-based LDH materials are promising electrocatalysts for the OER.

In this study, we reported an unprecedented nanostructured and multifunctional trimetallic NiVCe-based hydroxide, which exhibited enhanced stability and good performance as a positive electrode for HSCs, as well as electrocatalytic activity for OER, and for quantification of hydrogen peroxide, on account of the incorporation of Ce^{3+} and V^{5+} ions into the Ni(OH)$_2$ matrix. The new nanomaterial was carefully characterized by electrochemical techniques, including cyclic voltammetry (CV) and electrochemical impedance spectroscopy (EIS), as well as X-ray diffractometry (XRD) and transmission (TEM), and scanning transmission electron microscopy (STEM), where morphological and structural information were obtained. Additionally, elemental and chemical analyses were obtained by X-ray photoelectron spectroscopy (XPS).

MATERIALS AND METHODS

All reagents and solvents were of analytical grade and used as received. Glycerin, isopropyl alcohol, n-butyl alcohol, and KOH were purchased from Synth. Nickel acetate tetrahydrate and cerium acetate hydrate were obtained from Sigma-Aldrich. All

aqueous solutions were prepared with ultrapure deionized water from a MilliQ purification system (DI-water, $\rho \geq 18.2$ MΩ cm). All measurements were performed without oxygen removal and at ambient conditions.
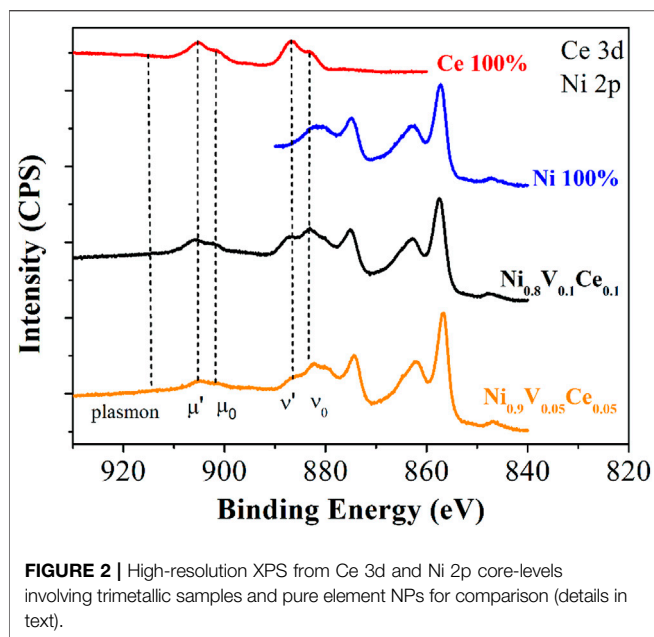
Preparation of α-Ni(OH)$_2$ and $Ni_{0.9}V_{0.05}Ce_{0.05}$-Layered Double Hydroxide Nanoparticles

The suspensions of α-Ni(OH)$_2$ and the unprecedented $Ni_{1-x-y}V_xCe_y$-LDH NPs (x = y = 0.05 or 0.10) were prepared as reported previously (Assis et al., 2020; Azeredo et al., 2021) by dissolving the total of 4.82 mmol of the metal acetates (or metal chloride, in the case of vanadium ions) in 25 ml of glycerin at 50°C. After the dissolution of the metal salts, 9.64 mmol of KOH dissolved in 25 ml of anhydrous n-butanol was added dropwise into the stirred solution at room temperature.

Preparation of Electrodes

Fluorine-doped tin oxide (FTO) glass plates were carefully washed with isopropanol and water, dried in air, and in the sequence modified by spin-coating the suspensions of α-Ni(OH)$_2$ and $Ni_{0.9}V_{0.05}Ce_{0.05}$-LDH NPs, at 2,500 rpm. These electrodes were then dried under vacuum at 80°C for 120 min. Such modified FTO electrodes were evaluated using CV, EIS, and galvanostatic charge-discharge (GCD). GCD curves were registered using larger modified FTO glass electrodes (geometric area ~4 cm^2) prepared as discussed earlier by spin-coating, applying a suitable volume of NP suspension (containing 3–8 mg) on the surface, and heating to 80°C.

The fabrication of the screen-printed electrode (SPE) is shown in **Scheme 1**. A cheap, flexible, and commercially available polyethylene terephthalate foil was used as a substrate to

FIGURE 2 | High-resolution XPS from Ce 3d and Ni 2p core-levels involving trimetallic samples and pure element NPs for comparison (details in text).

compose the SPEs. Ag/AgCl conductive ink was used to provide the reference electrode and the contact pads of the three electrodes to promote conductivity. Graphite ink loaded with 25 weight% of $Ni_{0.9}Ce_{0.05}V_{0.05}$-LDH NPs was screen-printed to build the working (WE) and counter (CE) electrodes. The fabrication process was simplified using the same ink in WE and CE, especially because similar results were observed for the SPE using a CE printed only with graphite ink (**Scheme 1A**). After that, the ink layer was dried at 85°C for 10 min in a Breville oven. A "blue tape" (adhesive) was used to define the active area of the electrodes, as well as to insulate the wire connections. The final dimensions of the SPE sensor were 3×1 cm (length *vs.* width). The surface area of the WE was ~12 mm^2, and the dimensions of the entire sensor were 3×1 cm (length *vs.* width), as shown in the design drawing (**Scheme 1B**) and photography (**Scheme 1C**) of the electrochemical analytical devices. The electrochemical measurements were carried out after properly connecting each of the electrodes (WE, reference electrode, and CE) to a potentiostat.

Instruments and Apparatus

The samples were characterized by XRD in a Bruker D2 Phaser equipment with a Cu Kα source (λ = 1.5418 Å as the source wavelength, voltage = 30 kV, current = 15 mA, step = 0.05°), in the 2θ range 5–70°. The samples were prepared by depositing the materials on glass slips and vacuum drying at 80°C. TEM and STEM images of the nanocomposites were obtained in JEOL JEM-2100 FEG equipment with an applied accelerating voltage of 200 kV. The samples were prepared on lacey carbon copper grids (Ted Pella) by dispersing 3 μl of an NP suspension diluted in DI-water. The relative amounts of nickel, vanadium, and cerium were measured by inductively coupled plasma optical emission spectrometry (Arcos/Spectro) using the solutions obtained by dissolving the concentrated dispersions of $Ni_{1-x-y}V_xCe_y$-LDH with a 0.1 mol L^{-1} nitric acid solution.

CV, GCD, and EIS measurements were carried out using an EcoChemie Autolab PGSTAT30 potentiostat/galvanostat and a conventional three-electrode cell constituted by an Ag/AgCl (3.0 mol L^{-1} KCl) reference, a platinum plate counter, and a modified FTO WE. For the batch injection analysis (BIA) experiments, amperometric detection was chosen, being the modified electrode positioned at the bottom of the three-dimensional-printed electrochemical BIA cell (Squissato et al., 2017; Rocha et al., 2018a). To perform the injections, a battery-powered Eppendorf electronic micropipette (Multipette® stream) was used, which allows injections with volumes and rates between 10 and 1,000 μl and flow rates from 28 to 345 μl s^{-1}. The injections mentioned earlier were carried out in a wall jet configuration (inverted position in relation to the working electrode with a distance of approximately 2 mm) (Rocha et al., 2018b). Electrochemical impedance spectra were recorded in the range from 0.01 to 50,000 Hz, modulating the frequency of a sinusoidal potential wave (amplitude = 10 mV) superimposed to a DC potential.

XPS was performed in a SPECS Phoibos 150 high-resolution hemispherical analyzer with multichannel detection using an Al K_α X-ray source (1,486.6 eV) with 180 W, operating at a 10^{-8} mbar base pressure, in normal emission, and constant pass energy (60 eV for the survey and 25 eV for high-resolution spectra). The hydroxide films were deposited on the native silicon oxide of silicon wafers that were glued to the sample holder with conductive carbon tape. The samples were inserted in a load-lock chamber to degas for 12 h before transferring to the XPS chamber. The obtained data were fitted assuming Shirley-type background and Lorentzian peaks numerically convoluted with a normalized Gaussian function with a fixed full-width half maximum of ~1.2 eV that describes the instrumental broadening.

RESULTS AND DISCUSSIONS

Structural and Morphological Characterization of $Ni_{1-x-y}V_xCe_y$-Layered Double Hydroxide Nanoparticle

In the last decade, the sol-gel method reported by Tower (Tower, 1924) has been extensively explored in the preparation of mono- and bimetallic hydroxides with a potential application, especially as electrochemical sensors (Azeredo et al., 2019; Azeredo et al., 2020) or electrodes for HSCs (Gonçalves et al., 2018a; Gomes et al., 2019). However, to the best of our knowledge, this is the first time that this method has been used to obtain multifunctional trimetallic hydroxides, reporting the unprecedented trimetallic NiVCe-based hydroxide (**Figure 1A**).

The relative amounts of nickel, vanadium, and cerium in the $Ni_{1-x-y}V_xCe_y$-LDH sol in the as-prepared materials were determined by inductively coupled plasma optical emission spectrometry. The relative Ni:V:Ce molar ratio measured for the $Ni_{0.9}V_{0.05}Ce_{0.05}$-LDH was 90.3:4.9:4.8, in good agreement with the expected values (90, 5, and 5%, respectively). In addition, the layered structure of $Ni(OH)_2$ and $Ni_{0.9}V_{0.05}Ce_{0.05}$-LDH NPs (**Figure 1A**) was confirmed by XRD
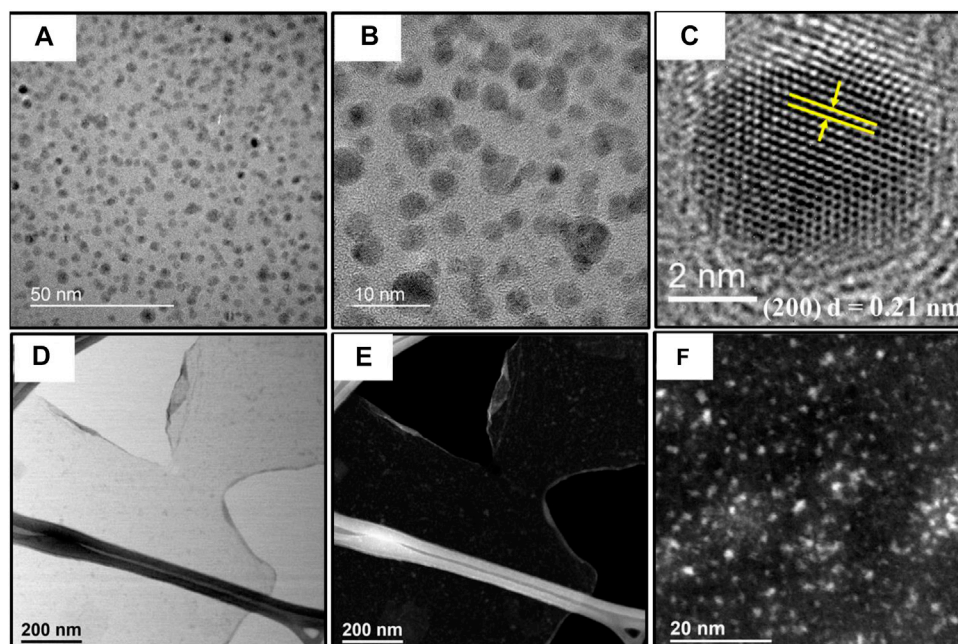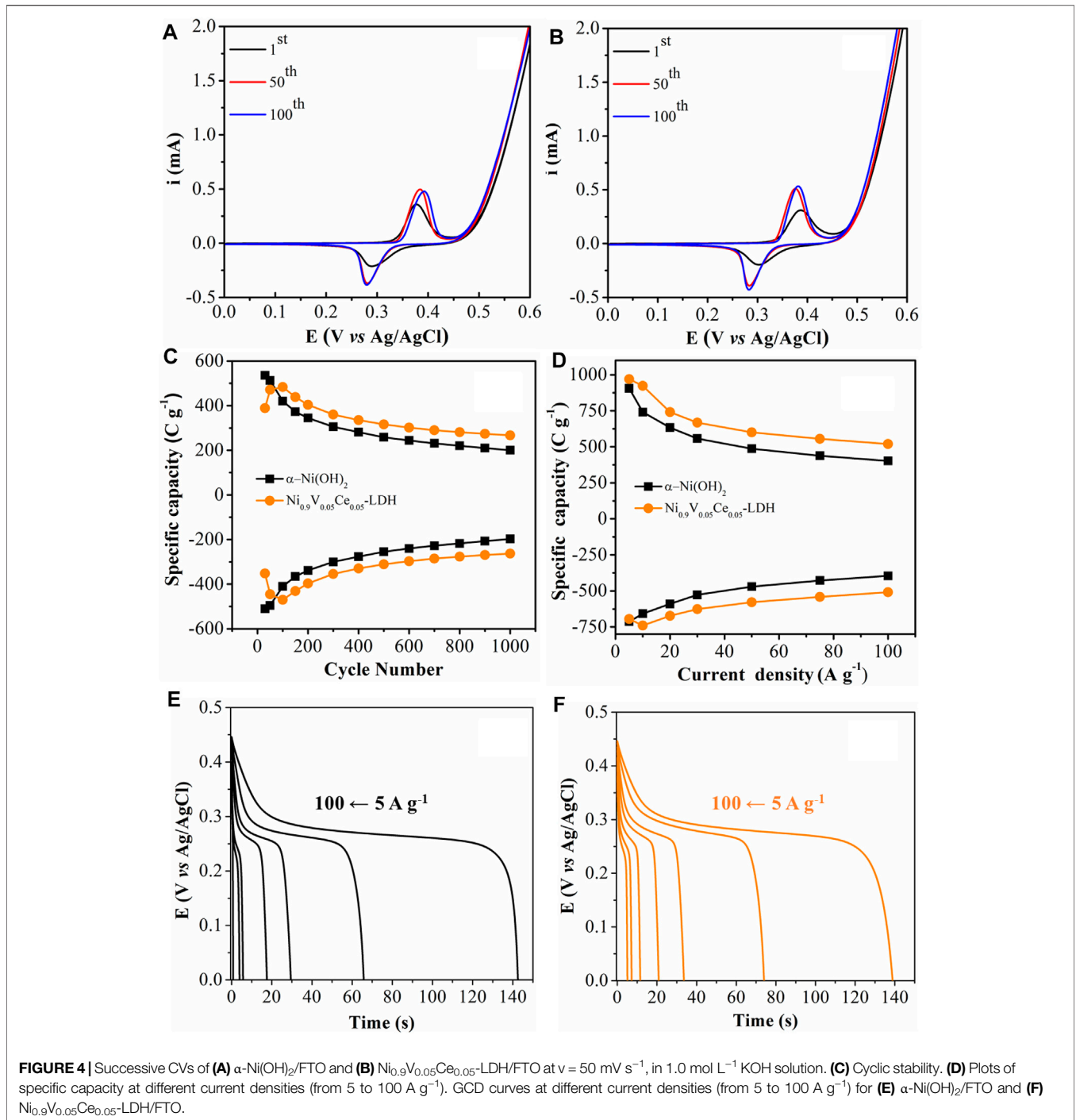
FIGURE 3 | (A, B) TEM images of $Ni_{0.9}V_{0.05}Ce_{0.05}$-LDH NPs/GO with magnification growing from left to right. **(C)** HRTEM of trimetallic oxide NPs formed *in situ* after dehydroxylation/dehydration reaction induced by electron beam. **(D)** Bright field-STEM image showing $Ni_{0.9}V_{0.05}Ce_{0.05}$-LDH NPs dispersed on GO surface and **(E)** same image in **(D)** in HAADF mode. **(F)** Higher magnification HAADF-STEM image of $Ni_{0.9}V_{0.05}Ce_{0.05}$-LDH NPs.

measurements (**Figure 1B**). The $Ni(OH)_2$ NPs presented a peak at 10.5° (8.45 Å), indexed to the (003) plane assigned to the turbostratic alpha-phase [α-$Ni(OH)_2$], as reported in the literature (Gonçalves et al., 2018b) [JCPDS no. 38-0175, α-$Ni(OH)_2 \cdot 0.75H_2O$]. Similarly, the presence of the basal reflections (003) in the $Ni_{0.9}V_{0.05}Ce_{0.05}$-LDH diffractogram at 10.5° (8.45 Å) evidences the formation of the LDH structure, where the apparent lower intensity and broadness of that diffraction peak are characteristics of a less crystalline material owing to rather smaller size nanoparticles (Azeredo et al., 2021). However, when the amount of vanadium ions precursor (VCl_3) is greater than five atom%, for example, in the case of bimetallic $Ni_{0.9}V_{0.1}$-LDH (**Supplementary Figure S1A**) and trimetallic $Ni_{0.8}V_{0.1}Ce_{0.1}$-LDH (**Supplementary Figure S1B**), the formation of KCl is noteworthy. In this case, a second phase indexed to the face-centered cubic KCl structure with peaks at 2θ = 28.37, 40.54, and 58.64°, which were indexed to (200), (220), and (400), respectively (Agarwal et al., 2017), was also recorded.

For a comprehensive chemical characterization of the formed trimetallic hydroxide NPs, XPS analysis was used. **Supplementary Figure S2** demonstrates the presence of the expected elements resulting from synthesis. Because the pure elements, Ni, V, and Ce, can produce multi- and complex phases depending on the synthesis conditions, it is worth studying the synthesis product from the pure elements for the sake of comparison. **Supplementary Figure S3** displays high-resolution XPS from Ni 2p, V 2p, and Ce 3d from 100% Ni, V, and Ce NPs samples. In the case of Ni 2p (**Supplementary Figure S3A**), the fitting procedure reveals a single-phase consistent with lamellar $Ni(OH)_2$ that has strong components

at 857.1 and 874.7 eV related to Ni $2p_{3/2}$ and Ni $2p_{1/2}$, respectively. The line shape, satellite structure, and peak positions are in good agreement with previous results from the literature (Xiong et al., 2017). **Supplementary Figure S3B** displays V 2p core-levels. Unfortunately, it has an important coincidence with O 1s satellites peaks promoted by the Al $K_{\alpha3,4}$ radiation. Despite that, the comprehensive fitting procedure, which has constrained the relative peak position and peak intensity, has been able to correctly untangle the information from V 2p. Taking into account the narrow linewidth and peak position at 517.5 eV for the V $2p_{3/2}$, one concludes for a single-phase consistent with V^{5+}, suggesting the formation of V_2O_5 (Preśniak-Welenc et al., 2016). Finally, **Supplementary Figure S3C** displays high-resolution XPS for Ce 3d core levels, which displays a complex structure of multiplets. There are four main feature peaks named ν_0 and ν' (882.8 and 886.5 eV) associated to Ce $3d_{5/2}$ and μ_0 and μ' (901.3 and 905.1 eV) associated with Ce $3d_{3/2}$. The relative peak position, as well as peak intensity, are well-known characteristics for the correct identification of Ce^{3+} or Ce^{4+} phases as demonstrated by Allahgholi et al. (2015). Furthermore, only the Ce^{+4} phase shows a characteristic plasmon structure around 917 eV. Therefore, our data are consistent with solely Ce^{3+}. Moreover, the line shape is also consistent with particle sizes between 1.4 and 2.4 nm, as previously reported by Allahgholi et al. (2015), which were also confirmed by TEM measurements (**Supplementary Figure S4**).

As we know the results from the single elements NPs, now in **Figure 2**, we can qualitatively compare the results for Ni 2p and Ce 3d core-levels for two trimetallic samples, $Ni_{0.9}V_{0.05}Ce_{0.05}$-

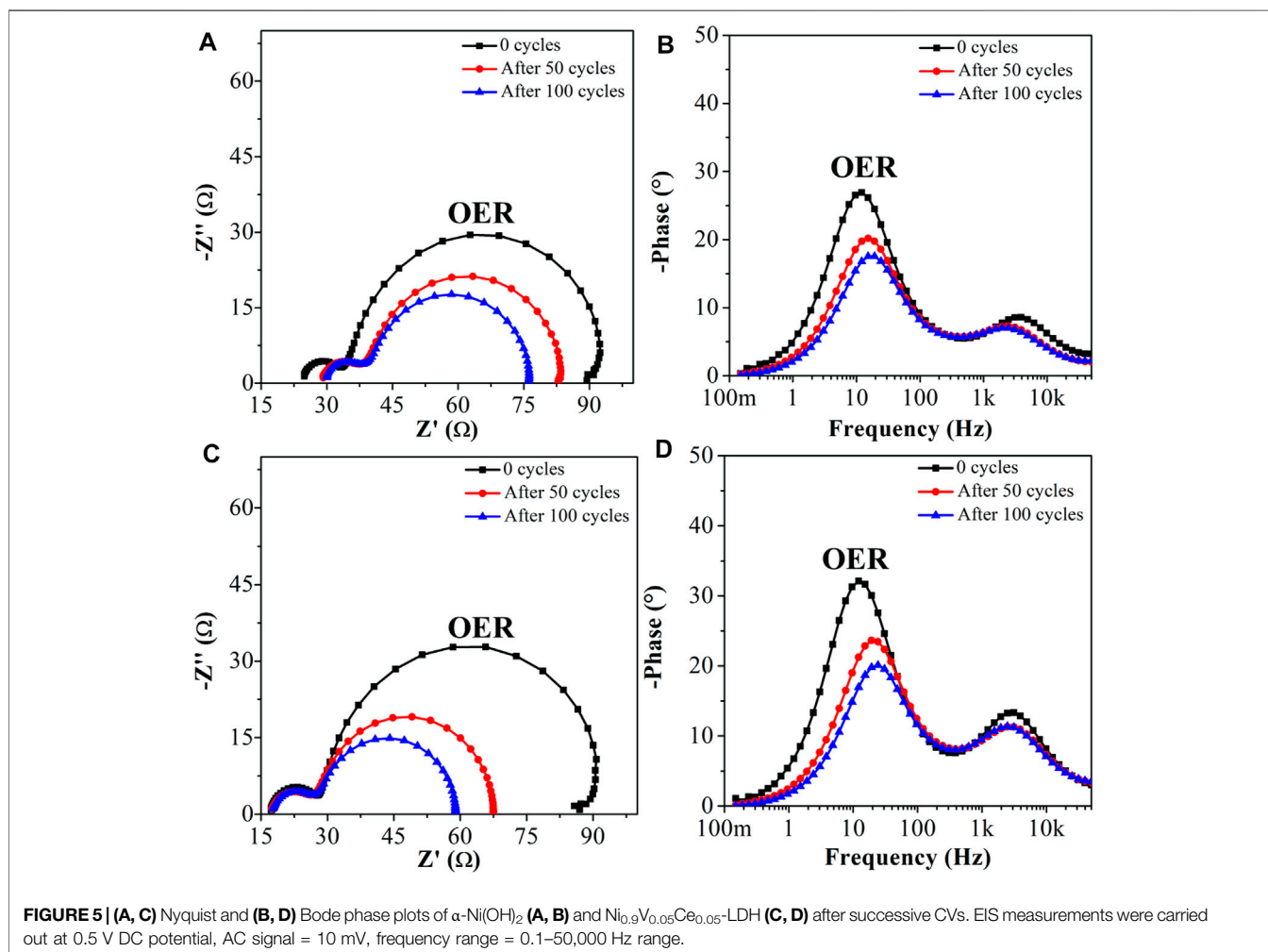FIGURE 4 | Successive CVs of **(A)** α-Ni(OH)$_2$/FTO and **(B)** Ni$_{0.9}$V$_{0.05}$Ce$_{0.05}$-LDH/FTO at v = 50 mV s^{-1}, in 1.0 mol L^{-1} KOH solution. **(C)** Cyclic stability. **(D)** Plots of specific capacity at different current densities (from 5 to 100 A g^{-1}). GCD curves at different current densities (from 5 to 100 A g^{-1}) for **(E)** α-Ni(OH)$_2$/FTO and **(F)** Ni$_{0.9}$V$_{0.05}$Ce$_{0.05}$-LDH/FTO.

LDH and Ni$_{0.8}$V$_{0.1}$Ce$_{0.1}$-LDH NPs. For the Ni, as a major element in the compound, the Ni 2p contributions are almost coincident for the three samples. Ce 3d$_{5/2}$ has partial overlap with the Ni 2p$_{1/2}$. Despite that, we can identify v$_0$, v', μ$_0$, and μ' peaks at almost the same position displayed in the pure Ce NPs. We might wonder if the NPs are formed by separated phases of Ni and Ce NPs instead of layered hydroxides formation. If separated phases are the case, we should be able to use the same peak positions, line widths, and relative peak intensities to fit the

complex structure. **Supplementary Figure S5** shows our attempt to fit the spectrum of Ni$_{0.8}$V$_{0.1}$Ce$_{0.1}$-LDH NPs using such constraints. The result demonstrates that extra structures are presented, suggesting the formation of a trimetallic hydroxide.

The formation of Ni$_{0.9}$V$_{0.05}$Ce$_{0.05}$-LDH NPs can be confirmed in the TEM/high-resolution transmission electron microscopy (HRTEM) images [**Figures 3A, B**, the NPs were designely prepared by depositing them on graphene oxide (GO) nanosheets], showing spherical shape with 4–6-nm diameter
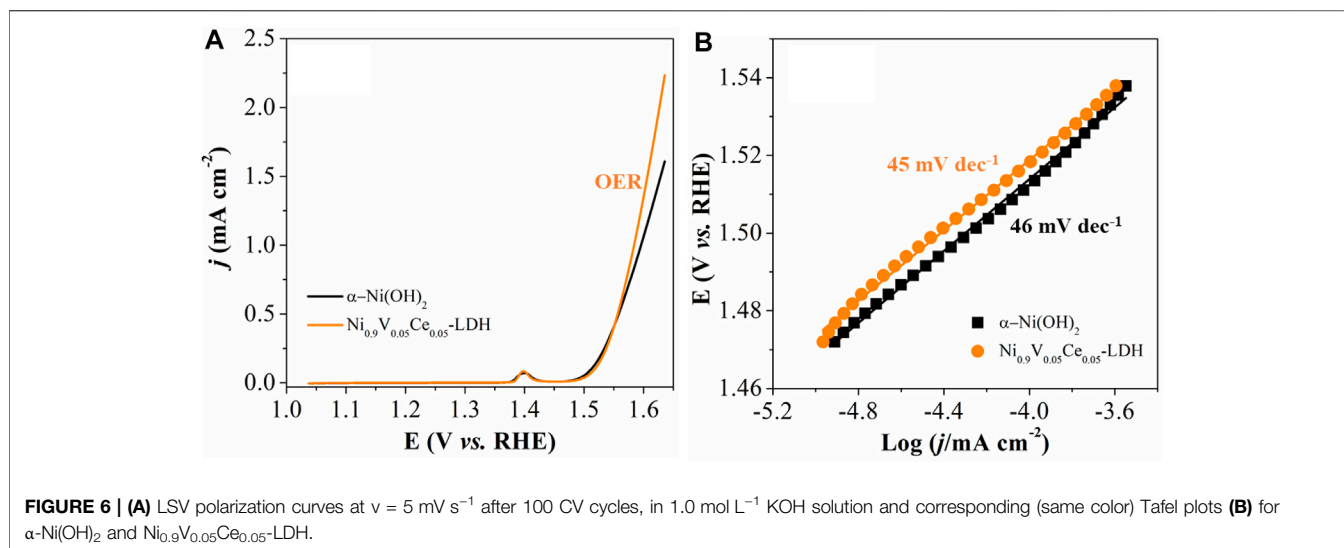
TABLE 1 | Comparison of pertinent electrochemical parameters of bi- and trimetallic metal hydroxide-based materials and their performance as cathode material.

Electrode material	Specific charge (C g^{-1})	Potential window V (Ref. electrode)	Rate capability in %retention (current density range)	Ref.
Ni$_{0.9}$V$_{0.05}$Ce$_{0.05}$-LDH	740 at 10 A g^{-1}	0.0–0.5 V (vs. Ag/AgCl)	68.7% (10–100 A g^{-1})	This work
Ni$_{0.80}$V$_{0.20}$-LDH	711 at 1 A g^{-1}	0.0–0.5 V (vs. Ag/AgCl)	~77% (1–10 A g^{-1})	Tyagi et al. (2019)
Ni$_{0.75}$Mn$_{0.25}$(OH)$_2$	417 at 25 A g^{-1}	0.0–0.47 V (vs. Ag/AgCl)	73.1% (4–100 A g^{-1})	Gomes et al. (2019)
Ni-Zn hydroxide/rGO	615.4 at 1 A g^{-1}	0.0–0.4 V (vs. SCE)	62.3% (1–30 A g^{-1})	Du et al. (2021)
NiCo-LDH/Ti$_3$C$_2$T$_x$	635.7 at 1 A g^{-1}	0.0–0.5 V (vs. Hg/HgO)	60.1% (1–20 A g^{-1})	Wang et al. (2021)
NiCo-LDH	312.9 at 1 A g^{-1}	0.0–0.4 V (vs. Ag/AgCl)	—	Liu et al. (2020)
CoS$_x$@NiCo-LDH	680.8 at 25 A g^{-1}	0.0–0.4 V (vs. Ag/AgCl)	76% (1–10 A g^{-1})	Liu et al. (2020)
NiCoAl-LDH/V$_4$C$_3$Tx	627 at 1 A g^{-1}	0.0–0.5 V (vs. Ag/AgCl)	47.8% (1–20 A g^{-1})	Wang et al. (2019b)
CoNiFe-LDH	360 at 0.4 A g^{-1}	−0.2–0.4 V (vs. Ag/AgCl)	51% (0.4–10 A g^{-1})	Rohit et al. (2021)
α-NiCoMn–OH	757 at 1 A g^{-1}	0.0–0.52 V (vs. Hg/HgO)	48.7% (1–50 A g^{-1})	Zhu et al. (2019)

FIGURE 5 | (A, C) Nyquist and **(B, D)** Bode phase plots of α-Ni(OH)$_2$ **(A, B)** and Ni$_{0.9}$V$_{0.05}$Ce$_{0.05}$-LDH **(C, D)** after successive CVs. EIS measurements were carried out at 0.5 V DC potential, AC signal = 10 mV, frequency range = 0.1–50,000 Hz range.

and no significant signs of agglomeration. In addition, the HRTEM images shown in **Figure 3C** are consistent with NPs with a high degree of crystallinity, as supported by the presence of reflection fringes assigned to the (200) diffraction planes of NiO (JCPDS no. 73–1523). At this moment, it is important to note that the dehydration process and consequent *in situ* formation of the

respective metal oxide NPs are quite common for this type of material, facilitated by the local heating and the high vacuum in the sample chamber. On the other hand, in contrast to TEM images, STEM images have even smaller NPs on GO, indicating that local heating can also induce the coalescence of nanoparticles, as confirmed by STEM-bright field (transmitted

FIGURE 6 | (A) LSV polarization curves at v = 5 mV s^{-1} after 100 CV cycles, in 1.0 mol L^{-1} KOH solution and corresponding (same color) Tafel plots **(B)** for α-Ni(OH)$_2$ and Ni$_{0.9}$V$_{0.05}$Ce$_{0.05}$-LDH.

electrons, BF, **Figure 3D**) and STEM-dark field images (scattered electrons in high-angle annular dark-field-HAADF, **Figures 3E, F**).

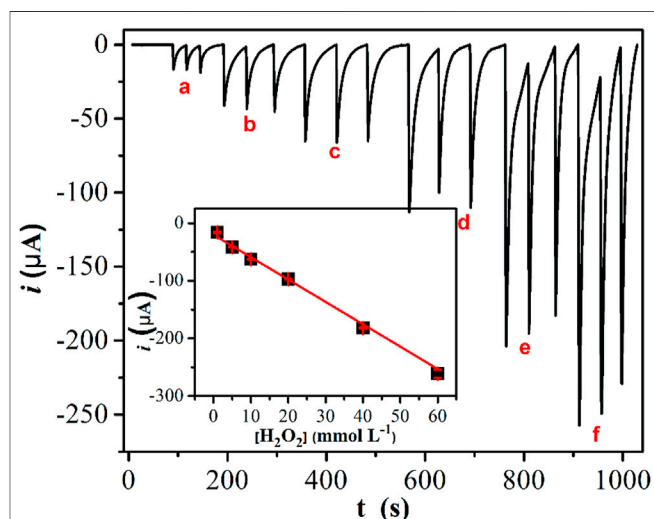## Ni$_{1-x-y}$V$_x$Ce$_y$-Layered Double Hydroxide as Electrode Material for Hybrid Supercapacitors

The electrochemical behavior of Ni$_{0.9}$V$_{0.05}$Ce$_{0.05}$-LDH and some bimetallic (Ni$_{0.95}$Ce$_{0.05}$-LDH and Ni$_{0.95}$V$_{0.05}$-LDH), as well as for α-Ni(OH)$_2$ analog modified FTO electrodes, were evaluated by CV. The CVs were recorded in the range of 0.0 to +0.6 V *vs.* Ag/AgCl (3.0 mol L^{-1} KCl), at a scan rate of 50 mV s^{-1}, using 1.0 mol L^{-1} KOH solution as the background electrolyte. For all electrodes, the CVs exhibited a well-defined pair of waves associated with the Ni^{2+}(OH)$_2$/Ni^{3+}(OOH) process (**Figure 4**). In addition, for the α-Ni(OH)$_2$, the anodic peak potential (i_{ap}) started to shift to more positive potentials, and the peak intensity decreased relatively fast after 50 continuous CVs (**Figure 4A**), typical of the conversion process of the nanomaterial from alpha to β-Ni(OH)$_2$ (Gonçalves et al., 2017). In contrast, the Ni$_{0.9}$V$_{0.05}$Ce$_{0.05}$-LDH exhibited a stable i_{ap} and a small potential shift during the 100 redox cycles (**Figure 4B**). This enhanced stability, also observed for bimetallic nickel/cerium LDH NPs (Gonçalves et al., 2017), probably is a result of the structural disorder induced to α-Ni(OH)$_2$ by cerium (III) cations (Gonçalves et al., 2017).

Complementarily, the robustness of the modified electrodes was evaluated during 1,000 consecutive GCD processes at 50 A g^{-1} in the 0.0 to +0.60 V *vs.* Ag/AgCl (3.0 mol L^{-1} KCl) range and monitoring the evolution of their specific charge as a function of the number of cycles (**Figure 4C**). In fact, similar to the results obtained by CV, the Ni$_{0.9}$V$_{0.05}$Ce$_{0.05}$-LDH/FTO electrode showed an increase in the specific charge up to the 100th cycle, retaining approximately 55% of the specific charge at the end of 1,000 cycles. In turn, the α-Ni(OH)$_2$/FTO electrode shows charge retention of approximately 37% as a result of its

conversion to β-Ni(OH)$_2$, confirming the greater stability of the trimetallic hydroxide in relation to the GCD cycles.

Considering the application, for example, in HSCs, the positive electrode materials should possess high specific capacity with a good rate capability. Interestingly, the plots shown in **Figure 4D** indicates that the maximum specific charge for Ni$_{0.9}$V$_{0.05}$Ce$_{0.05}$-LDH/FTO is 740 C g^{-1} at 10 A g^{-1} (discharge process) and displays the charge retention of 68.7% at 100 A g^{-1}, demonstrating that the trimetallic NPs can be able to withstand discharge rates as high as 100 A g^{-1}. As expected, the α-Ni(OH)$_2$/FTO electrode showed maximum specific capacity at the lowest applied current density (712 C g^{-1} at 5 A g^{-1}), retaining only 55.4% of specific capacity at 100 A g^{-1}. Furthermore, the electrochemical signature of both

FIGURE 7 | BIAgram constituted by triplicated injections of increasing concentrations of H$_2$O$_2$ [a) 1.0 × 10^{-3} mol L^{-1}; b) 5.0 × 10^{-3} mol L^{-1}; c) 1.0 × 10^{-2} mol L^{-1}; d) 2.0 × 10^{-2} mol L^{-1}, e) 4.0 × 10^{-2} mol L^{-1}, f) 6.0 × 10^{-2} mol L^{-1}]. Background electrolyte: 0.1 mol L^{-1} KCl. BIA operational conditions: working potential: 0.8 V; volume of injection: 150 µl; dispensing rate: 120 µl s^{-1}. Inset represents the respective analytical curve.

TABLE 2 | Analytical features obtained for determination of H_2O_2 using BIA technique.

Analyte	Linear range (mmol L^{-1})	Sensitivity (µA $mmol^{-1}$ L)	LOD[a] (µmol L^{-1})	% RSD (n = 5)		R^2
H_2O_2	1–60	4.9 ± 0.18	24.3	7.6[b]	5.7[c]	0.992

Sample	Found (mmol L^{-1})	Fortified (mmol L^{-1})	Recovery (mmol L^{-1})	Recovery (%)
Mouthwash	25.8 ± 0.3	10.0	35.0 ± 2.0	97.6 ± 7.0

[a]According to International Union of Pure and Applied Chemistry.
[b]5 mmol L^{-1}.
[c]20 mmol L^{-1}.

electrode materials show GCD curves characterized by a plateau (**Figures 4E, F**), typical of battery-type materials (Gonçalves et al., 2020b).

The electrochemical behavior of the trimetallic $Ni_{0.9}V_{0.05}Ce_{0.05}$-LDH was compared with other materials based on bimetallic and trimetallic hydroxide described in the literature and listed in **Table 1**. For instance, the maximum specific capacity for $Ni_{0.9}V_{0.05}Ce_{0.05}$-LDH/FTO is comparable with trimetallic α-NiCoMn−OH with a flower-like structure reported by Zhu et al. (2019) (757 C g^{-1} at 1 A g^{-1}) but with better charge retention capacity. In fact, the $Ni_{0.9}V_{0.05}Ce_{0.05}$-LDH comparatively presented high specific capacity at much larger current densities without any conductive-based material, as shown in **Table 1**. It is also relevant to mention that this excellent performance at high energy densities may be related to nanostructuration that leads to fast redox kinetics due to improved surface area and short diffusion pathways of the electrolyte in the NPs (Gonçalves et al., 2016).

$Ni_{1-x-y}V_xCe_y$-Layered Double Hydroxide as Electrode Material for Oxygen Evolution Reaction

The CVs showing high currents at potentials above 0.5 V vs. Ag/AgCl (**Figures 4A, B**) and the smaller specific discharge capacity at 5 A g^{-1} compared with 10 A g^{-1} (aforementioned, **Figure 4D**) demonstrate that the trimetallic hydroxide presented in this work also provides electrocatalytic activity for OER and will be parsed as a proof of concept.

This electrocatalytic property can be easily analyzed and monitored by EIS. The Nyquist plot and Bode phase spectra of α-Ni(OH)$_2$ after successive CVs [CVs performed range in the 0.0 to +0.6 V vs. Ag/AgCl $_{(3.0\ mol\ L^{-1}\ KCl)}$] display two semicircles (**Figure 5A**). The first activated process was assigned to the $Ni^{2+}(OH)_2/Ni^{3+}(OOH)$ electrochemical reaction (at high frequencies, 500–30,000 Hz), whereas the second one was associated with the OER catalyzed by the NPs (at lower frequencies, 0.1–100 Hz). It is interesting to highlight that the impedance of the OER (second) process decreased significantly after successive CVs, as confirmed by the decrease of the corresponding semicircle diameter and a simultaneous displacement of the associated peak in the Bode phase plot to higher frequencies (**Figure 5B**), as a result of the increased activation of a greater number of active sites and the improvement of the electrolyte diffusion. In comparison with

pure α-Ni(OH)$_2$, the higher stability of the $Ni_{0.9}V_{0.05}Ce_{0.05}$-LDH NPs is confirmed by the unchanging of the diameter assigned to the $Ni^{2+}(OH)_2/Ni^{3+}(OOH)$ electrochemical reaction at high frequencies and series cell resistance (R_s) (**Figures 5C, D**), as already noted in the CV experiments (**Figures 4A, B**). In fact, for the pure α-Ni(OH)$_2$ (**Figure 5A**), the R_s increases quite significantly and may be related to the inherent resistance of the material due to the transition from the alpha to the beta phase.

To confirm proof-of-concept of electrocatalytic performance of the prepared NPs, linear sweep voltammetry (LSV) measurements were carried out in 1.0-M KOH electrolyte using a standard three-electrode system (**Figure 6A**). The Tafel slope shown in **Figure 6B** derived from LSV curves is also an important parameter to evaluate the electrocatalyst reaction kinetics, which was calculated by the plot of potential against log (J) (Ahn et al., 2021). The $Ni_{0.9}V_{0.05}Ce_{0.05}$-LDH electrocatalyst showed a Tafel slope of 47 mV dec^{-1}, whereas that for the α-Ni(OH)$_2$ was 46 mV dec^{-1}, Tafel slope values similar to those reported for other NiV-LDHs (Liu et al., 2019; Bao et al., 2020), NiCoMn-LDH (Liu et al., 2021), NiCoFe-LDH (Zhang et al., 2020), and NiFeV-LDHs (Dinh et al., 2018; Li et al., 2018; Wang et al., 2019a) based electrocatalysts, indicating that both electrocatalysts are promising for OER.

$Ni_{1-x-y}V_xCe_y$-Layered Double Hydroxide Screen-Printed Electrode for the Electrochemical Detection of Hydrogen Peroxide

$Ni_{0.9}V_{0.05}Ce_{0.05}$-LDHs were synthesized (as described in the experimental section) and used in SPE modification aiming to improve the electrochemical detection of hydrogen peroxide (H_2O_2) found at mouthwash sample (purchased in a local market). Initially, to achieve an improvement in the response of the modified SPE, it was submitted to a well-known electrochemical treatment process using NaOH 0.5 mol L^{-1} by first applying +1.4 V for 200 s, followed by the potential of −1.0 V for another 200 s (Rocha et al., 2020). After the electrochemical treatment mentioned earlier, an increase of around 30% in the reduction current of 15 mmol L^{-1} H_2O_2 (background electrolyte: KCl 0.1 mol L^{-1}) was observed.

Subsequently, H_2O_2 was determined using the BIA technique with amperometric detection (Rocha et al., 2018b). The parameters that affect this technique, such as detection potential, volume injected, and dispensing speed, were

carefully evaluated. The first parameter to be evaluated was the best working potential. This potential was chosen through hydrodynamic voltammetry (**Supplementary Figure S6**). In this experiment, potentials in the range between 0 and −1.0 V were evaluated. As can be seen in the **Supplementary Figure S6**, −0.8 V provided the highest current intensity and, in addition, the lowest standard deviation among all other potentials. Therefore, this potential was chosen for future measurements. After determining the better working potential, the other parameters related to the BIA technique were evaluated (volume and dispensing speed). **Supplementary Figure S7** displays that when a volume of 150 μl and an injection speed of 120 μl s^{-1} were used, greater current intensities were achieved, as well as lower standard deviations. These conditions were adopted in the following measurements.

After selecting the better parameters for performing the BIA technique, a study to establish a good linear range for the H_2O_2 detection in mouthwash liquids was carried out (**Figure 7**). Based on the result observed from six increasing H_2O_2 concentrations, a linear range up to 60 mmol L^{-1} was obtained following the equation: $i = -2.2-4.9C$, where i is the current (in μA), and C is the concentration of H_2O_2 (in mmol L^{-1}). The coefficient of correlation (R) was calculated as 0.997. The relative standard deviation found for the concentrations of 5 and 20 mmol L^{-1} were 7.6 and 5.7%, respectively, and a LOD value of 24.3 μmol L^{-1} was estimated following the International Union of Pure and Applied Chemistry recommendations.

To show the versatility of the proposed material, the determination of H_2O_2 was performed in a real complex mouthwash sample. A concentration of 25.8 ± 0.3 mmol L^{-1} H_2O_2 was found in the sample, a concentration that is very close to that reported by the fabricant (25 mmol L^{-1}) and closer to the expected value than the results related in previous work (Katic et al., 2019). Additionally, a recovery study was carried out using the standard addition method, achieving a satisfactory recovery value of around 98%. **Table 2** summarizes the results obtained.

CONCLUSION

This study is reported for the first time the preparation of a nanostructured multifunctional layered double hydroxide containing Ni, V, and Ce ions (Ni$_{1-x-y}$V$_x$Ce$_y$-LDH, where x = y = 0.05). The Ni$_{0.9}$V$_{0.05}$Ce$_{0.05}$-LDH NPs were characterized by XRD, XPS, TEM/STEM, and HRTEM, indicating the absence of segregation and the formation of a homogeneous trimetallic hydroxide constituted by ultra-small (nanoparticles with sizes of 2–3 nm). The electrochemical and electrocatalytic properties of this new material were carefully characterized by CV, LSV, and EIS measurements. The incorporation of V^{5+} and Ce^{3+} ions in the turbostratic α-Ni(OH)$_2$ enhanced their stability and electrochemical properties as compared with pure nickel hydroxide NPs. In fact, the trimetallic NPs exhibited the largest specific charge of 740 C g^{-1} at 10 A g^{-1} and decent charge retention of 68.7% at 100 A g^{-1} [α-Ni(OH)$_2$, 712 C g^{-1} at 5 A g^{-1}, retaining only 55.4% of specific capacity at 100 A g^{-1}]. Furthermore, the

OER activity of the trimetallic materials was confirmed by their low Tafel slope of 47 mV dec^{-1} as a proof-of-concept. In addition, the multifunctionality of the Ni$_{0.9}$V$_{0.05}$Ce$_{0.05}$-LDH is also shown as SPE for monitoring hydrogen peroxide directly in a relatively complex mouthwash real sample. The cost-effectiveness, low reagent consumption, and facile preparation associated with the possibility of mass production of these electrodes are great advantages of the proposed sensors. In conclusion, the trimetallic Ni$_{0.9}$V$_{0.05}$Ce$_{0.05}$-LDH here explored showed excellent perspectives as multifunctional materials for energy technologies, so as for constructing sensors with great potential for amperometric applications.

DATA AVAILABILITY STATEMENT

The original contributions presented in the study are included in the article/**Supplementary Material**; further inquiries can be directed to the corresponding authors.

AUTHOR CONTRIBUTIONS

JG and LA designed the research and analyzed the data. JG, IL, NA, DR, and AS performed the research and analyzed the data and wrote the manuscript. LA and JG contributed to the revisions.

FUNDING

ACKNOWLEDGMENTS

SUPPLEMENTARY MATERIAL

The Supplementary Material for this article can be found online at: https://www.frontiersin.org/articles/10.3389/fmats.2021.781900/full#supplementary-material

REFERENCES

Agarwal, M., Garg, S. K., Asokan, K., Kanjilal, D., and Kumar, P. (2017). Facile Synthesis of KCl:Sm3+ Nanophosphor as a New OSL Dosimetric Material Achieved through Charge Transfer between the Defect States. *RSC Adv.* 7, 13836–13845. doi:10.1039/c6ra25237k

Ahn, I.-K., Lee, S.-Y., Kim, H. G., Lee, G.-B., Lee, J.-H., Kim, M., et al. (2021). Electrochemical Oxidation of boron-doped Nickel-Iron Layered Double Hydroxide for Facile Charge Transfer in Oxygen Evolution Electrocatalysts. *RSC Adv.* 11, 8198–8206. doi:10.1039/d0ra10169a

Allahgholi, A., Flege, J. I., Thieß, S., Drube, W., and Falta, J. (2015). Oxidation-State Analysis of Ceria by X-ray Photoelectron Spectroscopy. *Chemphyschem* 16, 1083–1091. doi:10.1002/cphc.201402729

Arif, M., Yasin, G., Luo, L., Ye, W., Mushtaq, M. A., Fang, X., et al. (2020). Hierarchical Hollow Nanotubes of NiFeV-Layered Double hydroxides@CoVP Heterostructures towards Efficient, pH-Universal Electrocatalytical Nitrogen Reduction Reaction to Ammonia. *Appl. Catal. B: Environ.* 265, 118559. doi:10.1016/j.apcatb.2019.118559

Assis, G. L., Gonçalves, J. M., Bernardes, J. S., and Araki, K. (2020). Nickel-Cerium Layered Double Hydroxide as Electrocatalyst for Glycerol Oxidation. *J. Braz. Chem. Soc.* 31, 2351–2359. doi:10.21577/0103-5053.20200131

Azeredo, N. F. B., Gonçalves, J. M., Lima, I. S., Araki, K., Wang, J., and Angnes, L. (2021). Screen-printed Nickel-Cerium Hydroxide Sensor for Acetaminophen Determination in Body Fluids. *Chemelectrochem* 8, 2505–2511. doi:10.1002/celc.202100417

Azeredo, N. F. B., Gonçalves, J. M., Rossini, P. O., Araki, K., Wang, J., and Angnes, L. (2020). Uric Acid Electrochemical Sensing in Biofluids Based on Ni/Zn Hydroxide Nanocatalyst. *Microchim Acta* 187, 379. doi:10.1007/s00604-020-04351-2

Azeredo, N. F. B., Rossini, P. O., Gonçalves, J. M., Assis, G. L., Araki, K., and Angnes, L. (2019). Nanostructured Mixed Ni/Pt Hydroxides Electrodes for BIA-Amperometry Determination of Hydralazine. *J. Taiwan Inst. Chem. Eng.* 95, 475–480. doi:10.1016/j.jtice.2018.08.033

Bao, W., Xiao, L., Zhang, J., Deng, Z., Yang, C., Ai, T., et al. (2020). Interface Engineering of NiV-LDH@FeOOH Heterostructures as High-Performance Electrocatalysts for Oxygen Evolution Reaction in Alkaline Conditions. *Chem. Commun.* 56, 9360–9363. doi:10.1039/d0cc03760e

Dinh, K. N., Zheng, P., Dai, Z., Zhang, Y., Dangol, R., Zheng, Y., et al. (2018). Ultrathin Porous NiFeV Ternary Layer Hydroxide Nanosheets as a Highly Efficient Bifunctional Electrocatalyst for Overall Water Splitting. *Small* 14, 1703257. doi:10.1002/smll.201703257

Du, Y., Li, G., Ye, L., Che, C., Yang, X., and Zhao, L. (2021). Sandwich-like Ni-Zn Hydroxide Nanosheets Vertically Aligned on Reduced Graphene Oxide via MOF Templates towards Boosting Supercapacitive Performance. *Chem. Eng. J.* 417, 129189. doi:10.1016/j.cej.2021.129189

Gomes, A. P., Gonçalves, J. M., Araki, K., and Martins, P. R. (2019). Enhancement of Stability and Specific Charge Capacity of Alpha-Ni(OH) 2 by Mn(II) Isomorphic Substitution. *Energy Technol.* 7, 1800980. doi:10.1002/ente.201800980

Gonçalves, J. M., Alves, K. M., Gonzalez-Huila, M. F., Duarte, A., Martins, P. R., and Araki, K. (2018). Unexpected Stabilization of α-Ni(OH)2 Nanoparticles in GO Nanocomposites. *J. Nanomater.* 2018, 5735609. doi:10.1155/2018/5735609

Gonçalves, J. M., da Silva, M. I., Toma, H. E., Angnes, L., Martins, P. R., and Araki, K. (2020). Trimetallic Oxides/hydroxides as Hybrid Supercapacitor Electrode Materials: a Review. *J. Mater. Chem. A* 8, 10534–10570. doi:10.1039/d0ta02939d

Gonçalves, J. M., Guimarães, R. R., Brandão, B. B. N. S., Saravia, L. P. H., Rossini, P. O., Nunes, C. V., et al. (2017). Nanostructured Alpha-NiCe Mixed Hydroxide for Highly Sensitive Amperometric Prednisone Sensors. *Electrochimica Acta* 247, 30–40. doi:10.1016/j.electacta.2017.06.166

Gonçalves, J. M., Guimarães, R. R., Nunes, C. V., Duarte, A., Brandão, B. B. N. S., Toma, H. E., et al. (2016). Electrode Materials Based on α-NiCo(OH)2 and rGO for High Performance Energy Storage Devices. *RSC Adv.* 6, 102504–102512. doi:10.1039/c6ra20317e

Gonçalves, J. M., Ireno da Silva, M., Angnes, L., and Araki, K. (2020). Vanadium-containing Electro and Photocatalysts for the Oxygen Evolution Reaction: a Review. *J. Mater. Chem. A* 8, 2171–2206. doi:10.1039/c9ta10857b

Gonçalves, J. M., Martins, P. R., Angnes, L., and Araki, K. (2020). Recent Advances in Ternary Layered Double Hydroxide Electrocatalysts for the Oxygen Evolution Reaction. *New J. Chem.* 44, 9981–9997. doi:10.1039/d0nj00021c

Gonçalves, J. M., Martins, P. R., Araki, K., and Angnes, L. (2021). Recent Progress in Water Splitting and Hybrid Supercapacitors Based on Nickel-Vanadium Layered Double Hydroxides. *J. Energ. Chem.* 57, 496–515. doi:10.1016/j.jechem.2020.08.047

Gonçalves, J. M., Matias, T. A., Saravia, L. P. H., Nakamura, M., Bernardes, J. S., Bertotti, M., et al. (2018). Synergic Effects Enhance the Catalytic Properties of alpha-Ni(OH)2-FeOCPc@rGO Composite for Oxygen Evolution Reaction. *Electrochimica Acta* 267, 161–169. doi:10.1016/j.electacta.2018.02.080

He, D., Cao, L., Huang, J., Kajiyoshi, K., Wu, J., Wang, C., et al. (2020). *In-situ* Optimizing the Valence Configuration of Vanadium Sites in NiV-LDH Nanosheet Arrays for Enhanced Hydrogen Evolution Reaction. *J. Energ. Chem.* 47, 263–271. doi:10.1016/j.jechem.2020.02.010

Katic, V., dos Santos, P. L., dos Santos, M. F., Pires, B. M., Loureiro, H. C., Lima, A. P., et al. (2019). 3D Printed Graphene Electrodes Modified with Prussian Blue: Emerging Electrochemical Sensing Platform for Peroxide Detection. *ACS Appl. Mater. Inter.* 11, 35068–35078. doi:10.1021/acsami.9b09305

Li, P., Duan, X., Kuang, Y., Li, Y., Zhang, G., Liu, W., et al. (2018). Tuning Electronic Structure of NiFe Layered Double Hydroxides with Vanadium Doping toward High Efficient Electrocatalytic Water Oxidation. *Adv. Energ. Mater.* 8, 1703341. doi:10.1002/aenm.201703341

Liu, B., Zhang, M., Wang, Y., Chen, Z., and Yan, K. (2021). Facile Synthesis of Defect-Rich Ultrathin NiCo-LDHs, NiMn-LDHs and NiCoMn-LDHs Nanosheets on Ni Foam for Enhanced Oxygen Evolution Reaction Performance. *J. Alloys Comp.* 852, 156949. doi:10.1016/j.jallcom.2020.156949

Liu, Q., Huang, J., Zhao, Y., Cao, L., Li, K., Zhang, N., et al. (2019). Tuning the Coupling Interface of Ultrathin Ni3S2@NiV-LDH Heterogeneous Nanosheet Electrocatalysts for Improved Overall Water Splitting. *Nanoscale* 11, 8855–8863. doi:10.1039/c9nr00658c

Liu, X., Ye, L., Du, Y., and Zhao, L. (2020). Metal Organic Framework Derived Core-Shell Hollow CoSx@NiCo-LDH as Advanced Electrode for High-Performance Supercapacitor. *Mater. Lett.* 258, 126812. doi:10.1016/j.matlet.2019.126812

Prześniak-Welenc, M., Karczewski, J., Smalc-Koziorowska, J., Łapiński, M., Sadowski, W., and Kościelska, B. (2016). The Influence of Nanostructure Size on V2O5 Electrochemical Properties as Cathode Materials for Lithium Ion Batteries. *Rsc Adv.* 6, 55689–55697.

Rocha, D. P., Cardoso, R. M., Tormin, T. F., de Araujo, W. R., Munoz, R. A. A., Richter, E. M., et al. (2018). Batch-injection Analysis Better Than Ever: New Materials for Improved Electrochemical Detection and On-Site Applications. *Electroanalysis* 30, 1386–1399. doi:10.1002/elan.201800042

Rocha, D. P., Silva, M. N. T., Cardoso, R. M., Castro, S. V. F., Tormin, T. F., Richter, E. M., et al. (2018). Carbon Nanotube/reduced Graphene Oxide Thin-Film Nanocomposite Formed at Liquid-Liquid Interface: Characterization and Potential Electroanalytical Applications. *Sensors Actuators B: Chem.* 269, 293–303. doi:10.1016/j.snb.2018.04.147

Rocha, D. P., Squissato, A. L., da Silva, S. M., Richter, E. M., and Munoz, R. A. A. (2020). Improved Electrochemical Detection of Metals in Biological Samples Using 3D-Printed Electrode: Chemical/electrochemical Treatment Exposes Carbon-Black Conductive Sites. *Electrochimica Acta* 335, 135688. doi:10.1016/j.electacta.2020.135688

Rohit, R. C., Jagadale, A. D., Shinde, S. K., Kim, D.-Y., Kumbhar, V. S., and Nakayama, M. (2021). Hierarchical Nanosheets of Ternary CoNiFe Layered Double Hydroxide for Supercapacitors and Oxygen Evolution Reaction. *J. Alloys Comp.* 863, 158081. doi:10.1016/j.jallcom.2020.158081

Rossini, P. d. O., Laza, A., Azeredo, N. F. B., Gonçalves, J. M., Felix, F. S., Araki, K., et al. (2020). Ni-based Double Hydroxides as Electrocatalysts in Chemical Sensors: A Review. *Trac Trends Anal. Chem.* 126, 115859. doi:10.1016/j.trac.2020.115859

Shao, M., Zhang, R., Li, Z., Wei, M., Evans, D. G., and Duan, X. (2015). Layered Double Hydroxides toward Electrochemical Energy Storage and Conversion: Design, Synthesis and Applications. *Chem. Commun.* 51, 15880–15893. doi:10.1039/c5cc07296d

Squissato, A. L., Silva, W. P., Del Claro, A. T. S., Rocha, D. P., Dornellas, R. M., Richter, E. M., et al. (2017). Portable Electrochemical System Using Screen-

Printed Electrodes for Monitoring Corrosion Inhibitors. *Talanta* 174, 420–427. doi:10.1016/j.talanta.2017.06.042

Tomboc, G. M., Kim, J., Wang, Y., Son, Y., Li, J., Kim, J. Y., et al. (2021). Hybrid Layered Double Hydroxides as Multifunctional Nanomaterials for Overall Water Splitting and Supercapacitor Applications. *J. Mater. Chem. A.* 9, 4528–4557. doi:10.1039/d0ta11606h

Tower, O. F. (1924). Note on Colloidal Nickel Hydroxide. *J. Phys. Chem.* 28, 176–178. doi:10.1021/j150236a009

Tyagi, A., Joshi, M. C., Shah, A., Thakur, V. K., and Gupta, R. K. (2019). Hydrothermally Tailored Three-Dimensional Ni-V Layered Double Hydroxide Nanosheets as High-Performance Hybrid Supercapacitor Applications. *ACS Omega* 4, 3257–3267. doi:10.1021/acsomega.8b03618

Wang, X., Li, H., Li, H., Lin, S., Bai, J., Dai, J., et al. (2019). Heterostructures of Ni-Co-Al Layered Double Hydroxide Assembled on V4C3MXene for High-Energy Hybrid Supercapacitors. *J. Mater. Chem. A.* 7, 2291–2300. doi:10.1039/c8ta11249e

Wang, Y., Shi, C., Chen, Y., Li, D., Wu, G., Wang, C., et al. (2021). 3D Flower-like MOF-Derived NiCo-LDH Integrated with Ti3C2Tx for High-Performance Pseudosupercapacitors. *Electrochimica Acta* 376, 138040. doi:10.1016/j.electacta.2021.138040

Wang, Z., Liu, W., Hu, Y., Xu, L., Guan, M., Qiu, J., et al. (2019). An Fe-Doped NiV LDH Ultrathin Nanosheet as a Highly Efficient Electrocatalyst for Efficient Water Oxidation. *Inorg. Chem. Front.* 6, 1890–1896. doi:10.1039/c9qi00404a

Xiong, D., Li, W., and Liu, L. (2017). Vertically Aligned Porous Nickel(II) Hydroxide Nanosheets Supported on Carbon Paper with Long-Term Oxygen Evolution Performance. *Chem. Asian J.* 12, 543–551. doi:10.1002/asia.201601590

Xu, H., Wang, B., Shan, C., Xi, P., Liu, W., and Tang, Y. (2018). Ce-Doped NiFe-Layered Double Hydroxide Ultrathin Nanosheets/Nanocarbon Hierarchical Nanocomposite as an Efficient Oxygen Evolution Catalyst. *ACS Appl. Mater. Inter.* 10, 6336–6345. doi:10.1021/acsami.7b17939

Zhang, M., Liu, Y., Liu, B., Chen, Z., Xu, H., and Yan, K. (2020). Trimetallic NiCoFe-Layered Double Hydroxides Nanosheets Efficient for Oxygen Evolution and Highly Selective Oxidation of Biomass-Derived 5-Hydroxymethylfurfural. *ACS Catal.* 10, 5179–5189. doi:10.1021/acscatal.0c00007

Zhou, P., Wang, C., Liu, Y., Wang, Z., Wang, P., Qin, X., et al. (2018). Sulfuration of NiV-Layered Double Hydroxide towards Novel Supercapacitor Electrode with Enhanced Performance. *Chem. Eng. J.* 351, 119–126. doi:10.1016/j.cej.2018.06.064

Zhu, Y., Huang, C., Li, C., Fan, M., Shu, K., and Chen, H. C. (2019). Strong Synergetic Electrochemistry between Transition Metals of α Phase Ni−Co−Mn Hydroxide Contributed superior Performance for Hybrid Supercapacitors. *J. Power Sourc.* 412, 559–567. doi:10.1016/j.jpowsour.2018.11.080